Formation of a sodium ring in Mercury's magnetosphere

Manabu Yagi, K. Seki, Y. Matsumoto, Dominique C. Delcourt, François Leblanc

Formation of a sodium ring in Mercury's magnetosphere

M. Yagi,[1] K. Seki,[1] Y. Matsumoto,[1] D. C. Delcourt,[2] and F. Leblanc[3]

[1]   We have performed a statistical analysis of exospheric sodium ion paths in Mercury's magnetosphere under northward interplanetary magnetic field conditions. Electric and magnetic field models used in the simulation were obtained from a global MHD simulation model, whereas the initial conditions of test Na^+ ions were derived from a sodium exosphere model. We observe the formation of a ring-shaped high-pressure region consisting of energetic sodium ions traveling around the planet close to the equatorial plane. The configuration of this "sodium ring" as well as the acceleration processes leading to its formation strongly depend on the solar wind conditions. When the dynamic pressure is low, most of the Na^+ are picked up in the magnetosphere and accelerated by the large-scale convective electric field. In contrast, in the case of high dynamic pressure, ions that are picked up in the magnetosheath and penetrate into the magnetosphere significantly contribute to the sodium ring. The configuration of this ring also depends upon the intensity of the solar wind electric field. Our analysis reveals that the pressure built by the Na^+ ions may be significant as compared to the MHD pressure around the planet.

Citation: Yagi, M., K. Seki, Y. Matsumoto, D. C. Delcourt, and F. Leblanc (2010), Formation of a sodium ring in Mercury's magnetosphere, *J. Geophys. Res.*, *115*, A10253, doi:10.1029/2009JA015226.

1. Introduction

[2]   Mariner 10 surprisingly discovered the existence of an intrinsic magnetosphere at Mercury. Though there are quadrupole and octupole moments [*Whang*, 1977], the intrinsic magnetic field is nearly dipolar with an intensity of about 350 nT at the equator [*Ness et al.*, 1975]. Recently, MESSENGER performed three flybys of Mercury, and the strength of the magnetic field was estimated to range between 240 and 270 nT at the equator [*Anderson et al.*, 2008]. Measurements from both Mariner 10 and MESSENGER also reveal phenomena similar to those occurring at Earth, such as substorm-like signatures [*Siscoe et al.*, 1975] or vortices driven by Kelvin-Helmholtz instability, plasmoid structures, and flux transfer events [*Slavin et al.*, 2008; *Slavin*, 2009].

[3]   While several characteristics seem to be common between Earth and Mercury's ionized environments, some critical differences have been pointed out. One of these differences is the absence of inner magnetosphere, plasmasphere and ring current regions. Mercury itself is relatively large compared to its magnetosphere, and a substantial portion of a rescaled model of the Earth's magnetosphere at Mercury begins inside the planet surface [*Slavin*, 2004]. The configuration of Mercury's magnetosphere also changes much more drastically than that of Earth with respect to solar wind conditions. This is due to the weak intrinsic magnetic field (about 1/1500 of the Earth's dipole moment intensity) and to the strong solar wind dynamic pressure (about 10 times larger at Mercury than at Earth). In extreme situations such as Coronal Mass Ejection (CME) events, Mercury's magnetopause may be pushed toward the surface, leading to a direct interaction of the solar wind with the planet surface. Another important difference between Mercury and Earth magnetospheres is the absence of atmosphere (and thus ionosphere) so that the current system at Mercury should be significantly different than the terrestrial one.

[4]   Although there is no thick atmosphere, several species have been identified in Mercury's exosphere [*McClintock et al.*, 2008], and ground based observations demonstrate the existence of a tenuous sodium exosphere [*Potter and Morgan*, 1985]. Detailed features such as a north-south asymmetry or an extended sodium tail, have also been observed [e.g., *Potter and Morgan*, 1997, 2002; *Kameda et al.*, 2009]. Monte Carlo simulations that describe the processes of ion-sputtering, photo stimulated desorption, thermal desorption, and micrometeoroid vaporization, have been performed to characterize the different components of the exosphere [*Leblanc and Johnson*, 2003; *Mura et al.*, 2007; *Leblanc and Johnson*, 2010]. As a matter of fact, though thin, the sodium exosphere may be a substantial source of magnetospheric plasma through photoionization process [*Leblanc et al.*, 2003] and MHD calculations taking into account these ions of planetary origin have been performed [*Kidder et al.*, 2008].

[5]   These observational evidences have stimulated a variety of simulations of the ionized environment of

[1]Solar-Terrestrial Environment Laboratory, Nagoya University, Nagoya, Japan.
[2]Laboratoire de Physique des Plasmas, Ecole Polytechnique-CNRS Observatoire de Saint-Maur, Saint Maur des Fosses, France.
[3]LATMOS/IPSL, Universitè Versailles Saint Quentin, CNRS, Verrières-le-Buisson, France.

Mercury. *Kabin et al.* [2000] reported north-south and dawn-dusk asymmetries in the magnetosphere using MHD simulation. They took into account realistic solar wind parameters, including strong IMF (interplanetary magnetic field) Bx and By which causes the asymmetries, consistent with Parker's spiral. These MHD simulations also emphasize the importance of the solar wind dynamic pressure and that of the IMF orientation for the overall structure of the magnetosphere [*Ip and Kopp*, 2002; *Kabin et al.*, 2008].

[6] MHD is a widely used approach to investigate the behavior of magnetospheric plasmas. However, in a small-scale magnetosphere like that of Mercury, kinetic effects linked to the finite Larmor radius of ions (in particular, heavy ones) cannot be neglected and MHD models are not fully appropriate to characterize the environment. Results of global 3-D hybrid simulations show several characteristics which cannot be described by MHD simulation such as a dawn-dusk asymmetry arising from drift motions of ions [*Kallio and Janhunen*, 2003] or the formation of a hot plasma ring around Mercury [*Travnicek et al.*, 2007]. Trajectory tracing of exospheric ions in model magnetosphere also highlighted an asymmetry between dawn and dusk sectors of the magnetosphere, as well as nonadiabatic effects during meandering motion in the neutral sheet [*Delcourt et al.*, 2003]. Precipitating sodium ions that are accelerated in the nightside magnetosphere may also produce secondary sodium ions or neutrals [*Ip*, 1987; *Leblanc et al.*, 2003]. Thus sodium ions of the exospheric origin likely play an important role in the dynamics of Mercury's magnetosphere.

[7] Statistical trajectory tracing has been used to examine the acceleration of ions and electrons [e.g., *Delcourt et al.*, 2005; 2007], which is one of the important problems in Mercury's magnetosphere [*Lundin et al.*, 1997; *Eraker and Simpson*, 1986]. However, the charged particle motion heavily depends upon the electric and magnetic field configuration. It is thus important to consider a realistic field model before addressing the motion of particles within such a magnetosphere. *Sarantos et al.* [2009] showed the results of test particle simulations in a global MHD simulation of Mercury's magnetosphere developed by [*Benna et al.*, 2010] under solar wind conditions based on the observation of MESSENGER. They discussed the importance of pickup ions in the magnetosheath, which can be a source of hot plasma in the magnetosphere.

[8] The goal of the present study is 1) to examine the basic structure of Mercury's magnetosphere in relation with a variety of solar wind conditions, and 2) to estimate the contribution of exospheric sodium ions to the magnetospheric dynamics. In section 2, we first show results of global MHD simulations of Mercury's magnetosphere under four different solar wind conditions with northward IMF. Using the electric and magnetic fields obtained with these MHD simulations, trajectory tracing of sodium ions in Mercury's magnetosphere is performed in section 3, and implications for Mercury's magnetosphere are discussed in section 4. The results are summarized in section 5.

2. MHD Simulation

[9] This section presents the electric and magnetic fields used for the systematic trajectory tracing, as obtained from our global MHD simulation model.

2.1. Description of the MHD Model

[10] The normalized basic equations solved in the MHD model are as follows:

$$\frac{\partial \rho}{\partial t} = -(\mathbf{V} \cdot \nabla)\rho - \rho(\nabla \cdot \mathbf{V}), \tag{1}$$

$$\frac{\partial \mathbf{V}}{\partial t} = -(\mathbf{V} \cdot \nabla)\mathbf{V} - \frac{1}{2\rho}\nabla P - \frac{1}{\rho}\mathbf{J} \times \mathbf{B} + \frac{1}{\rho R_e}\nabla^2 \mathbf{V}, \tag{2}$$

$$\frac{\partial P}{\partial t} = -(\mathbf{V} \cdot \nabla)P - \gamma P(\nabla \cdot \mathbf{V}), \tag{3}$$

$$\frac{\partial \mathbf{A}}{\partial t} = -\mathbf{E} - \nabla\phi, \tag{4}$$

where ρ, $\mathbf{V}$, P, $\mathbf{A}$, $\mathbf{B}$, $\mathbf{J}$, $\mathbf{E}$, and ϕ denote density, velocity, pressure, vector potential, magnetic field, current density, electric field, and scalar potential, respectively. In addition, $\mathbf{A}$, $\mathbf{B}$, $\mathbf{E}$, and $\mathbf{J}$ satisfy the following equations:

$$\mathbf{B} = \mathbf{B}_0 + \nabla \times \mathbf{A}, \tag{5}$$

$$\mathbf{J} = \nabla \times \mathbf{B} = \nabla(\nabla \cdot \mathbf{A}) - \nabla^2 \mathbf{A}, \tag{6}$$

$$\mathbf{E} = -\mathbf{V} \times \mathbf{B} + \frac{1}{R_b}\mathbf{J} = (\mathbf{V} \cdot \nabla)\mathbf{A} - (\nabla \mathbf{A}) \cdot \mathbf{V}$$
$$+ \frac{1}{R_b}\{\nabla(\nabla \cdot \mathbf{A}) - \nabla^2 \mathbf{A}\}. \tag{7}$$

$\mathbf{B}_0$ represents the dipole magnetic field which satisfies $\nabla \times \mathbf{B}_0 = 0$. R_e represents the Reynolds number which is defined as $R_e = V_A \Delta x/\mu$ where μ is the kinematic viscosity, and R_b is the magnetic Reynolds number defined by $R_b = \mu_0 V_A \Delta x/\eta$ where μ_0 is the magnetic permeability and η is the plasma resistivity. In this study, R_e and R_b are constant and set to 0.5 and 0.1, respectively. In equation (4), ϕ can be arbitrary determined, and we choose $\nabla \cdot \mathbf{A}$ for ϕ in order to keep $\nabla \cdot \mathbf{A}$ term small. This choice of ϕ improves the precision of $\mathbf{J} \times \mathbf{B}$ term in equation (2) [*Yagi et al.*, 2009]. To solve the advection term (the first term on the right-hand side of the equations (1)–(4), and (7)), we adopted a Rational-CIP algorithm which is known to be a low numerical dispersion scheme [*Yabe and Aoki*, 1991; *Xiao et al.*, 1996]. The nonadvection terms are solved by a fourth-order Runge-Kutta method for time advance and a fourth-order central difference for space discretization [*Yagi et al.*, 2009]. This model automatically satisfies the solenoidal property of the magnetic field so that we can avoid an artificial acceleration [*Brackbill and Barnes*, 1980].

[11] Inner boundary conditions of the planetary surface are applied for p, ρ, and V_t as $f_{r0-dr} = f_{r0+dr}$ and v_r as $f_{r0-dr} = -f_{r0+dr}$, where r_0 is the radius of Mercury and dr is the radial distance from the planetary surface. Vector potential $\mathbf{A}$ is difficult to define at the boundary because it is an integral quantity. In this study, we do not replace the value of vector potential but solve the induction equation (equation (4)) in the entire simulation domain including inside the planet. With these inner boundary conditions, waves are reflected
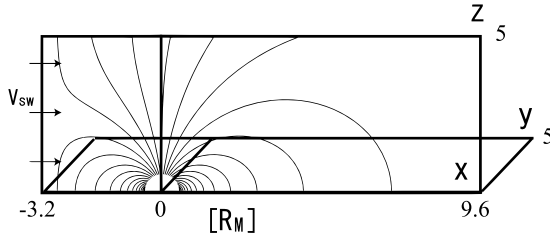
Figure 1. Schematic view of the simulation box. The x axis is set for the Sun-Mercury direction, the z axis is set for the dipole axis, and the y axis is set so as to form the right-handed system. Gray lines show the initial condition of intrinsic magnetic field.

and magnetic field lines are moved by the convection at the planetary surface. Equivalently, these inner boundary conditions assume Mercury to be a low conductive body. Spatial resolution is set as $\Delta x = 0.05 R_M$, where R_M is the radius of Mercury, i.e., 2440 km. The number of grid points is set as (nx, ny, nz) = (256, 100, 100) with regular Cartesian grid which corresponds to ranges of $-3.2 \leq X \leq 9.6\ R_M$, $0 \leq Y \leq 5 R_M$, $0 \leq Z \leq 5\ R_M$ in the real space as shown in Figure 1. We only solve the north-dawn sector of the magnetosphere in order to save computational costs. Free boundary conditions ($\frac{\partial f}{\partial x_i} = 0$ in the x_i direction) are applied to the outer boundaries except for the sunward one, in which each value is fixed to the solar wind parameters. For vector potential, $\frac{\partial A_i}{\partial x_i} = 0$, $\frac{\partial^2 A_{j,k}}{\partial x_i^2} = 0$ in the x_i direction are applied in order to satisfy free boundary condition for magnetic field. The time step Δt corresponds to 0.0035 seconds, which is determined to satisfy the CFL (Courant-Friedrich-Lewy) condition ($V_{max} \frac{\Delta t}{\Delta x} = 0.12$) at the pole. Initial conditions in the simulation box are set as $\rho = 10$ cm^{-3}, $\mathbf{V} = (0,0,0)$ km/s, and $P = 0.19$ nPa. Intrinsic magnetic field of Mercury $\mathbf{B}_0$ is given as follows.

$$B_{0x} = -\frac{\mu_0}{4\pi} \frac{M_H}{r^5} 3xz, \qquad (8)$$

$$B_{0y} = -\frac{\mu_0}{4\pi} \frac{M_H}{r^5} 3yz, \qquad (9)$$

$$B_{0z} = -\frac{\mu_0}{4\pi} \frac{M_H}{r^5} \left(3z^2 - r^2\right), \qquad (10)$$

where M_H is the dipole moment of 4.36×10^{19} Am^2 which is equivalent to 300 nT at equator [*Ness et al.*, 1975].

[12] We examined four different cases of solar wind conditions with northward IMF, as summarized in Table 1. In Case 1, density is relatively low for the perihelion. In Case 2, dynamic pressure is 4 times higher than in Case 1. In Cases 3 and 4, the dynamic pressure as well as the IMF strength is the same as in Case 2 but the solar wind speed (and thus the y component of the electric field) is different.

2.2. Results of Global MHD Simulations

[13] Figures 2 and 3 show snapshots of 4 cases of the global MHD simulations when the magnetosphere reached a quasi-steady state. In Case 1, the magnetopause and the bow shock in front of the magnetosphere are formed at $1.7 R_M$

and $2.3 R_M$, respectively. The locations of magnetopause and bow shock move to $1.4 R_M$ and $1.7 R_M$ in Cases 2, 3, and 4, that is closer to the planet than in Case 1. The similarity of the global configuration for Cases 2, 3, and 4, which have the same solar wind dynamic pressure indicates that, not unexpectedly, P_{dyn} plays a major role in defining the global structure of Mercury's magnetosphere. The locations of magnetopause and bow shock were estimated to be $1.6 R_M$ and $2.2 R_M$ by previous MHD simulation [*Kabin et al.*, 2000] and $1.4 R_M$ and $1.8 R_M$ using Mariner 10 observation [*Ogilvie et al.*, 1977]. The location of Mercury's subsolar magnetopause obtained in previous studies is listed in Table 2. The differences between these simulations are essentially caused by different solar wind conditions and different dipolar magnetic moment. It is apparent from Table 2 that our MHD simulation is in good agreement with previous studies.

[14] Figure 3 illustrates that, in all cases, similar convection patterns are obtained while the convection velocity slightly changes due to changes in the solar wind dynamic pressure. In all cases, the magnetic flux is transported from the flank side to the central nightside sector. In the tail region (that is, for $X > 2 R_M$), the flow is somewhat turbulent but almost tailward. On the other hand, there is a return flow that transports the flux back to the dayside. Though such a flow has a typical velocity smaller than 5 km/s, it plays an important role in the dynamics of the sodium ions, as will be seen in section 3.

3. Trajectory Tracings of Exospheric Ions

3.1. Simulation Model

[15] In order to examine the contribution of exospheric sodium ions to Mercury's magnetosphere, we performed trajectory tracing of test Na$^+$ in the electric and magnetic field models obtained from the above MHD simulations. Initial Na$^+$ conditions are determined from a model of Mercury's exosphere at perihelion conditions as illustrated in Figure 4 [*Leblanc et al.*, 2003]. This exosphere model is obtained by 3-D Monte Carlo simulations that take into account the four main ejection mechanisms of sodium atoms from the surface, namely: thermal desorption, photo stimulated desorption, micrometeoroid vaporization, and solar wind sputtering. We initially loaded about 230,000 test particles from each bin of the exosphere outside of the shadow of the planet (the shadow corresponds to the region between the two horizontal solid lines plotted in Figure 4). Initial velocity for each ion is also given by the exosphere model. Mass loading rate per cell is given by $F_i = f_{ion} N_i \Delta x^3$, where f_{ion}, N_i, Δx^3 are exosphere density of the sodium atoms (Figure 4), photoionization frequency (1.39×10^{-4} s [e.g., *Killen and Ip*, 1999]), and bin volume. We then follow these newly ionized particles by fourth-order Runge-Kutta

Table 1. Solar Wind Parameters of Cases 1–4[a]

	ρ (cm^{-3})	V_{sw} (km/s)	P_{dyn} (nPa)	IMF (nT)
Case 1	35	400	9.35	[0, 0, 10]
Case 2	140	400	37.4	[0, 0, 10]
Case 3	70	565	37.4	[0, 0, 10]
Case 4	35	800	37.4	[0, 0, 10]

[a]P_{dyn} is defined as $m_p \rho V_{SW}^2$, where m_P denotes the proton mass 1.67×10^{-27}.
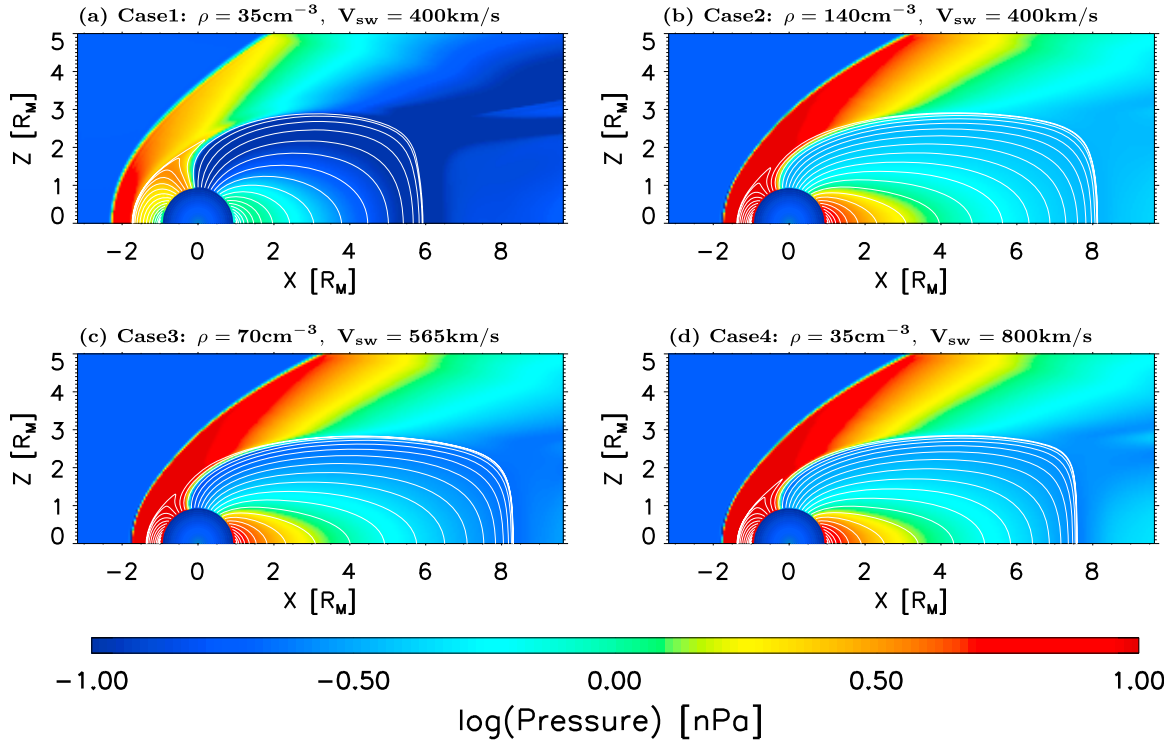
Figure 2. Snapshots of the global MHD simulation of Mercury's magnetosphere in the meridian plane at the quasi-static state for (a) Case 1, (b) Case 2, (c) Case 3, and (d) Case 4, respectively. White lines show the magnetic field lines and color codes represent pressure in a logarithmic scale.
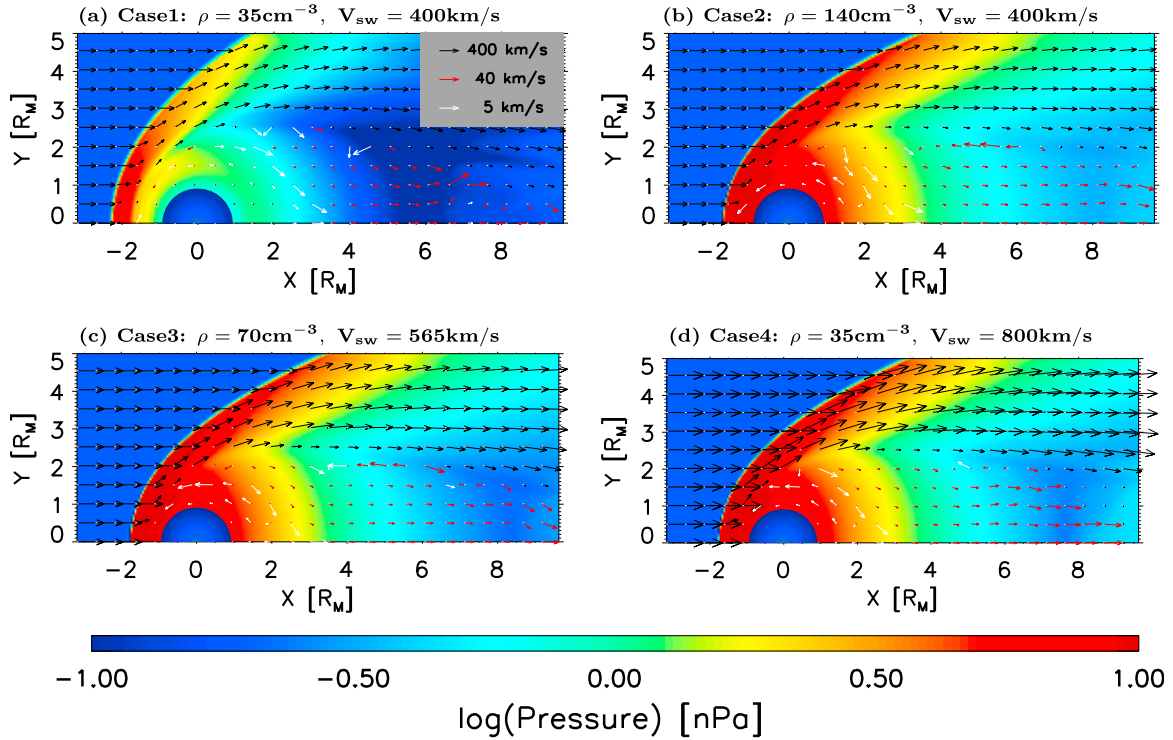
Figure 3. Snapshots of the global MHD simulation of Mercury's magnetosphere in the equatorial plane at the quasi-static state for (a) Case 1, (b) Case 2, (c) Case 3, and (d) Case 4, respectively. Pressure (color codes) and velocity vectors (arrows) in the equatorial plane are shown. Black arrows are for velocities larger than 40 km/s. Red arrows are for velocities between 5 and 40 km/s. White arrows are for velocities less than 5 km/s.

Table 2. Solar Wind Conditions and Calculated Location of the Subsolar Magnetopause for Previous Studies of Mercury's Magnetosphere[a]

	ρ (cm^{-3})	V_{sw} (km/s)	IMF (nT)	MP (R_M)
Travnicek et al. [2007]	73	600	[40, 23, 0]	1.2
Travnicek et al. [2007]	32	250	[18, 11, 0]	1.7
Kallio and Janhunen [2003]	76	430	[0, 0, 10]	1.4
Kabin et al. [2000]	73	430	[43, 16, 0]	1.6

[a]MP, magnetopause.

method until they exit the simulation box or encounter the planetary surface. Number density and pressure of the sodium ions were calculated as follows:

$$\rho = \Sigma_i (F_i t_i) / \Delta x^3, \tag{11}$$

$$\overline{V} = \Sigma_i (F_i t_i V_i) / (\rho \Delta x^3), \tag{12}$$

$$P = \Sigma_i \left(F_i t_i (V_i - \overline{V})^2 \right) / (\rho \Delta x^3), \tag{13}$$

where t_i, V_i, $\overline{V}$ and Δx^3 denote time of flight in the cell, average speed of ions in each bin, and the volume of each bin (which is the same as in the MHD simulation), respectively.

3.2. Formation of the "Sodium Ring"

[16] Figure 5 shows the sodium pressure and density profiles in the meridian and equatorial planes obtained by integrating the trajectory of exosphere originating Na$^+$ (Figure 4). In the meridian plane, sodium ions can be seen in the high-latitude lobe region. Because of their small energy, these ions hardly contribute to the pressure. In the equatorial plane, a narrow high-pressure region forms in the magnetosheath. This region consists of both pickup ions in the magnetosheath and ions escaping from the magnetosphere. The dawn-dusk asymmetry is due to finite Larmor radius effects. In particular, it can be seen that "ring shape" high-density and high-pressure region forms around the planet in the equatorial plane, the pressure outside of this region being almost negligible. Figure 6 shows the results of trajectory tracing in Case 2 (the high dynamic pressure case). Here because the magnetopause is pushed inward, the high-pressure ring that is still present on the dayside becomes narrower. This result is consistent with the 3-D hybrid simulations of [*Travnicek et al.*, 2007] although they considered protons. Note the lower pressure level in Case 2 as compared to Case 1. In addition, it can be seen in Figure 6 that another high-pressure sodium band forms upstream of the magnetopause. This latter feature can be explained by the trajectory of ions picked up in the solar wind region. These ions drift toward the electric field direction because the Larmor radius is larger than the simulation volume. In Cases 3 and 4 (Figures 7 and 8) that correspond to high speed solar wind cases, the pressure of the ring on the nightside becomes weaker. The ring is less extended in Case 4, though the pressure is higher than that of Case 2.

[17] In order to discuss the behavior of particles and how to form those high-pressure regions, we analyzed energy

distributions. Figure 9 shows energy distributions sampled at dayside, nightside, dawnside, and duskside. In Case 1 (Figure 9a), these distributions have peaks around 1 keV in all sampled regions. This ~1 keV population corresponds to ions experiencing westward gradient drift around the planet. In Cases 2, 3, and 4 (Figures 9b–9d), particles with energy up to 1 keV are distributed in a uniform manner, but a few particles are accelerated above 1 keV on the dayside. At dawnside, two populations can be seen in the energy distributions. One is around 1 keV as in Case 1, while the other corresponds to a more energetic population, up to 5 keV energy. The two populations are easy to see in Case 4 but difficult to distinguish in Cases 2 and 3 because these two energy distributions overlap. Energy distributions on the nightside and duskside have similar shapes but the density is smaller than on the dawnside. In addition, these populations depend largely on the solar wind electric field. This indicates that a large proportion of the drifting particles are lost by precipitation onto the planet while they are drifting from the dawnside to nightside. Acceleration up to keV can be explained by pickup acceleration by the magnetospheric convective electric field on the dayside. Still, another acceleration mechanism is needed to explain higher-energy ions (above keV).

3.3. Acceleration Mechanisms

[18] In order to understand the acceleration of sodium ions, we analyzed the motions of individual particles. Figure 10 shows the trajectory of a typical particle for each of the 4 above cases (left), together with energy variation as a function of time. In Case 1 (Figure 10a), the particle is initially launched at r = 1.5 R_M, MLT = 14, LAT = 0, and E = 0 eV, where r, MLT, LAT, and E denote radial distance, magnetic local time, latitude, and energy, respectively. The particle is first accelerated by the convection electric field. Once accelerated, the gradient drift speed exceeds the convection speed and the particle starts drifting around the planet. This particle effectively drifts for more than one h and ultimately impacts the planet surface. While drifting around the planet, the energy does not change significantly. This result is consistent with the energy distribution in Figure 9 showing a similar population ~1 keV at all local times.
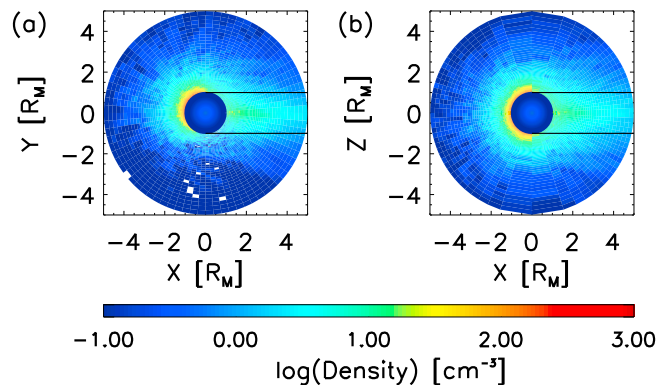
Figure 4. Spatial distribution of neutral sodium density obtained from Mercury's exosphere model [*Leblanc et al.*, 2003] in the (a) equatorial and (b) meridian plane, respectively.
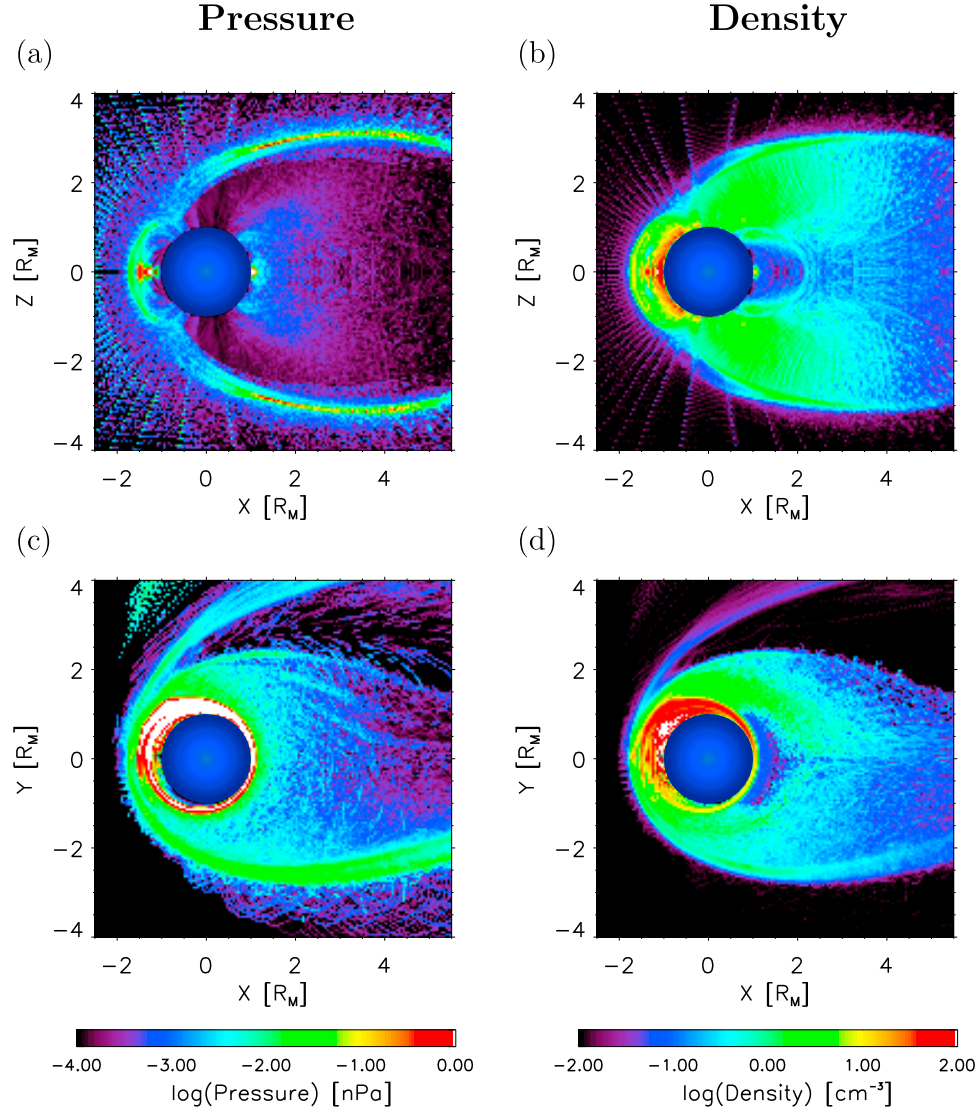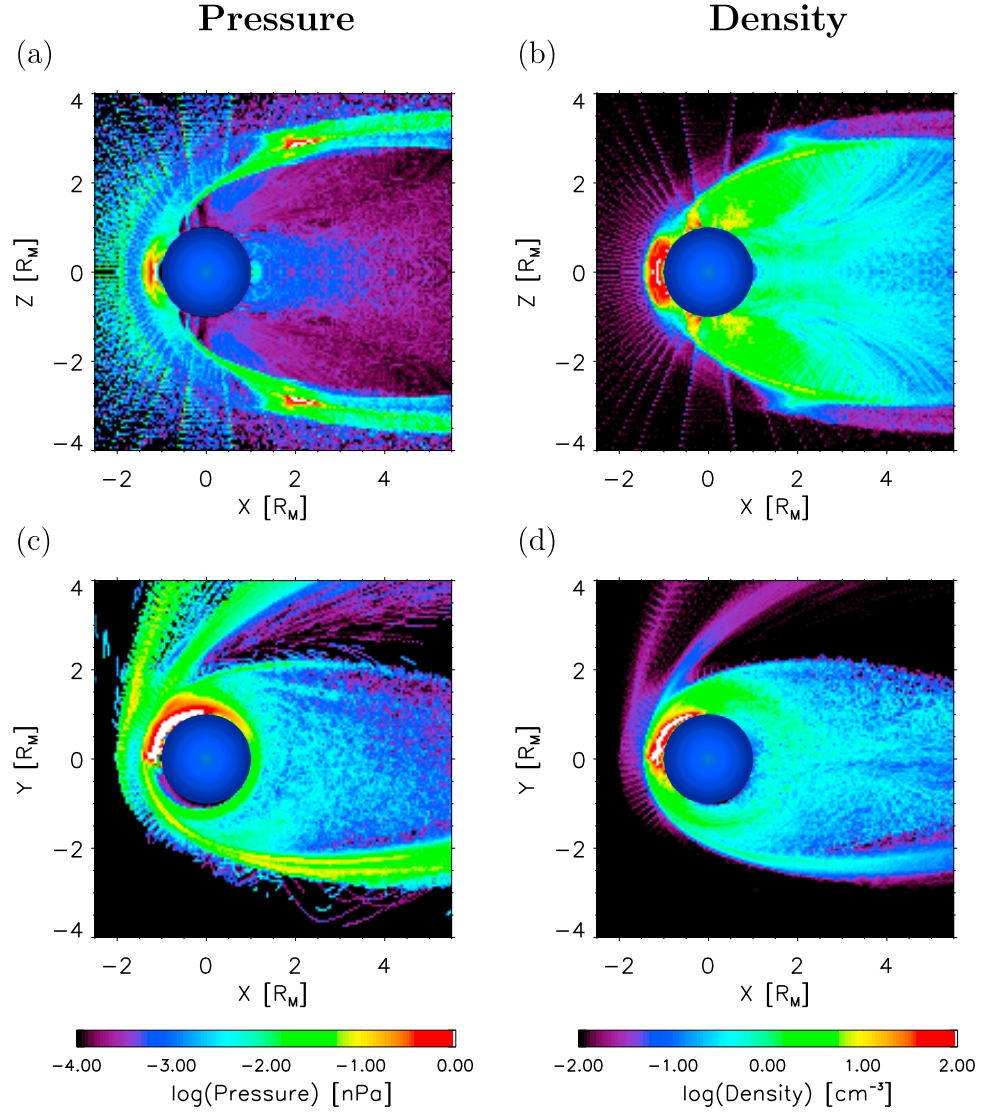
Figure 5. The results of statistical trajectory tracings of test sodium ions for Case 1. (left) The pressure and (right) the number density in logarithmic scales. (top) The profiles in the meridian plane and (bottom) the profiles in the equatorial plane.
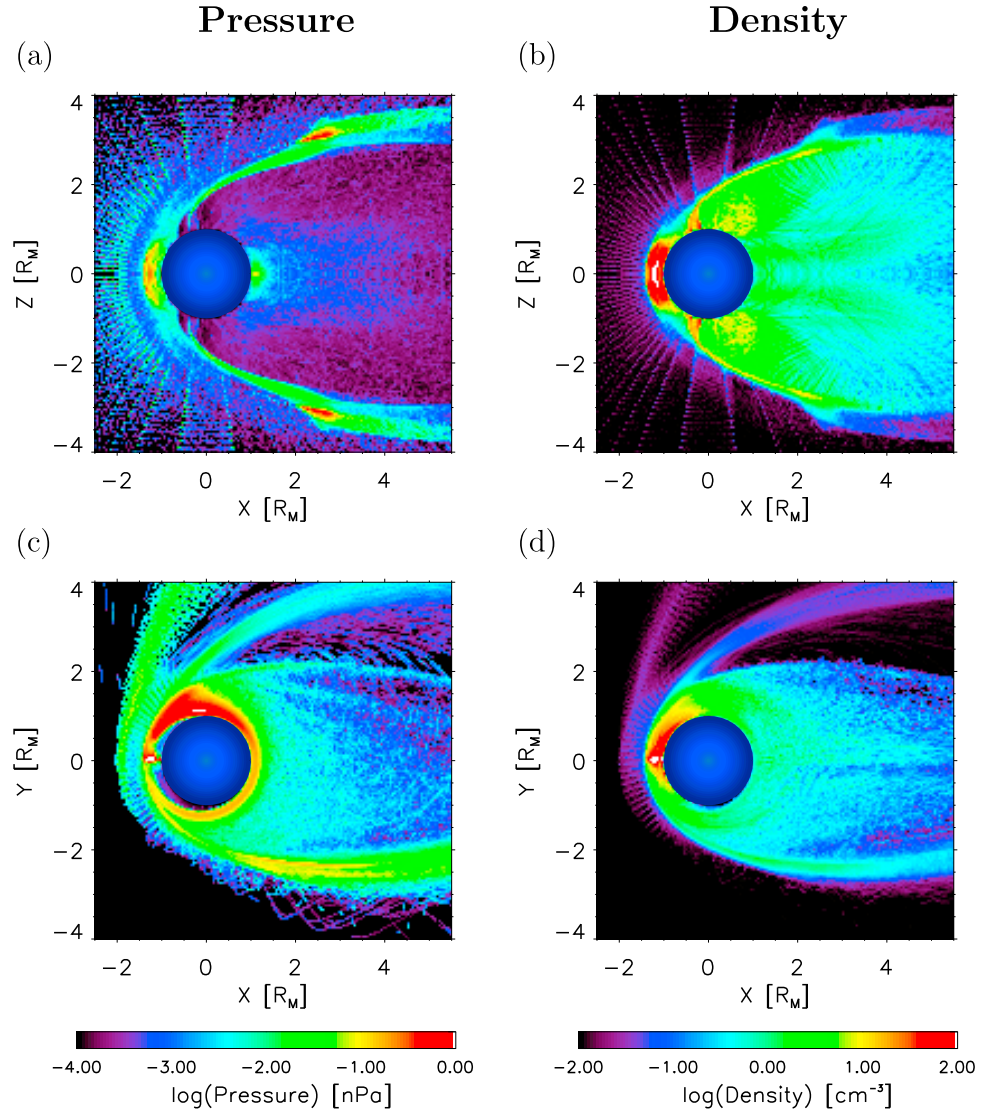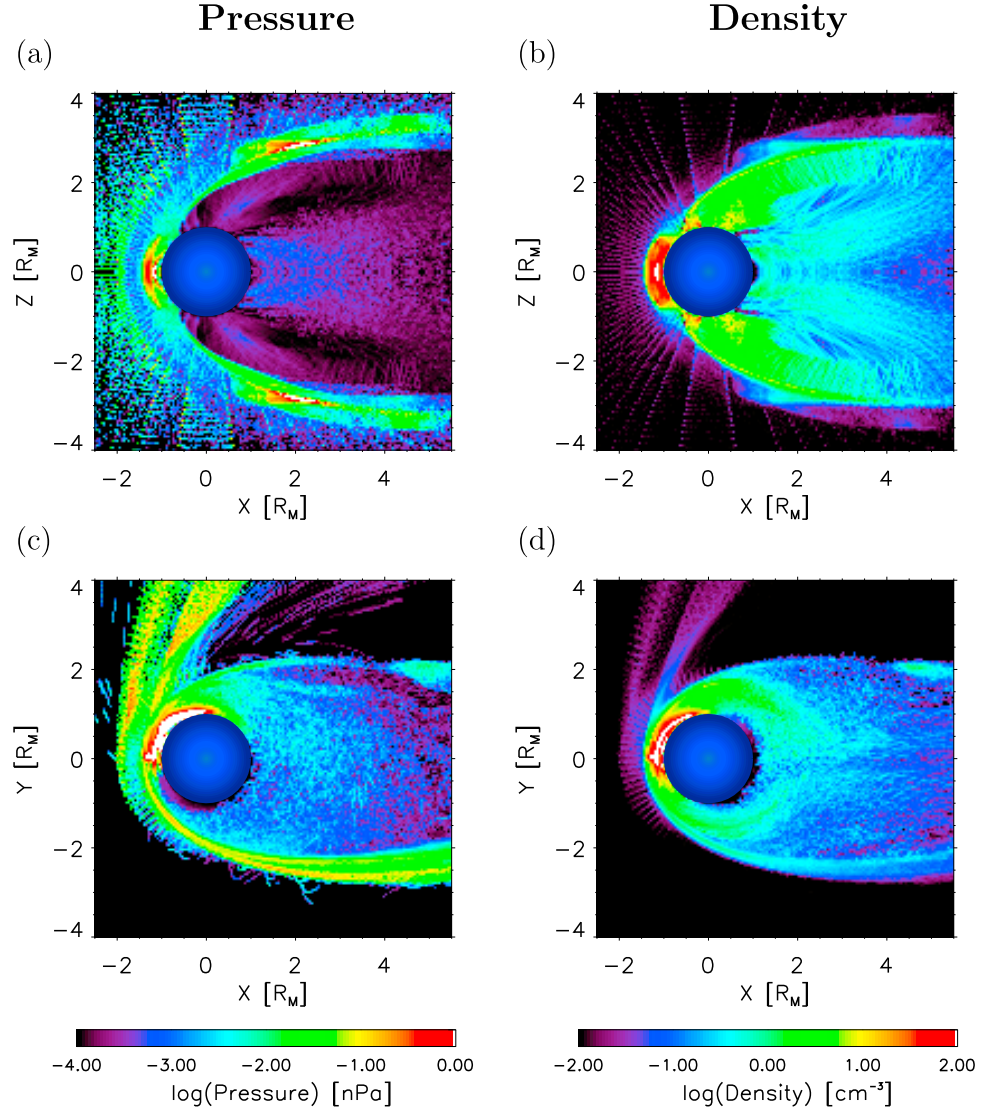
Figure 6. The results of statistical trajectory tracings of test sodium ions for Case 2. The format is the same as in Figure 5.
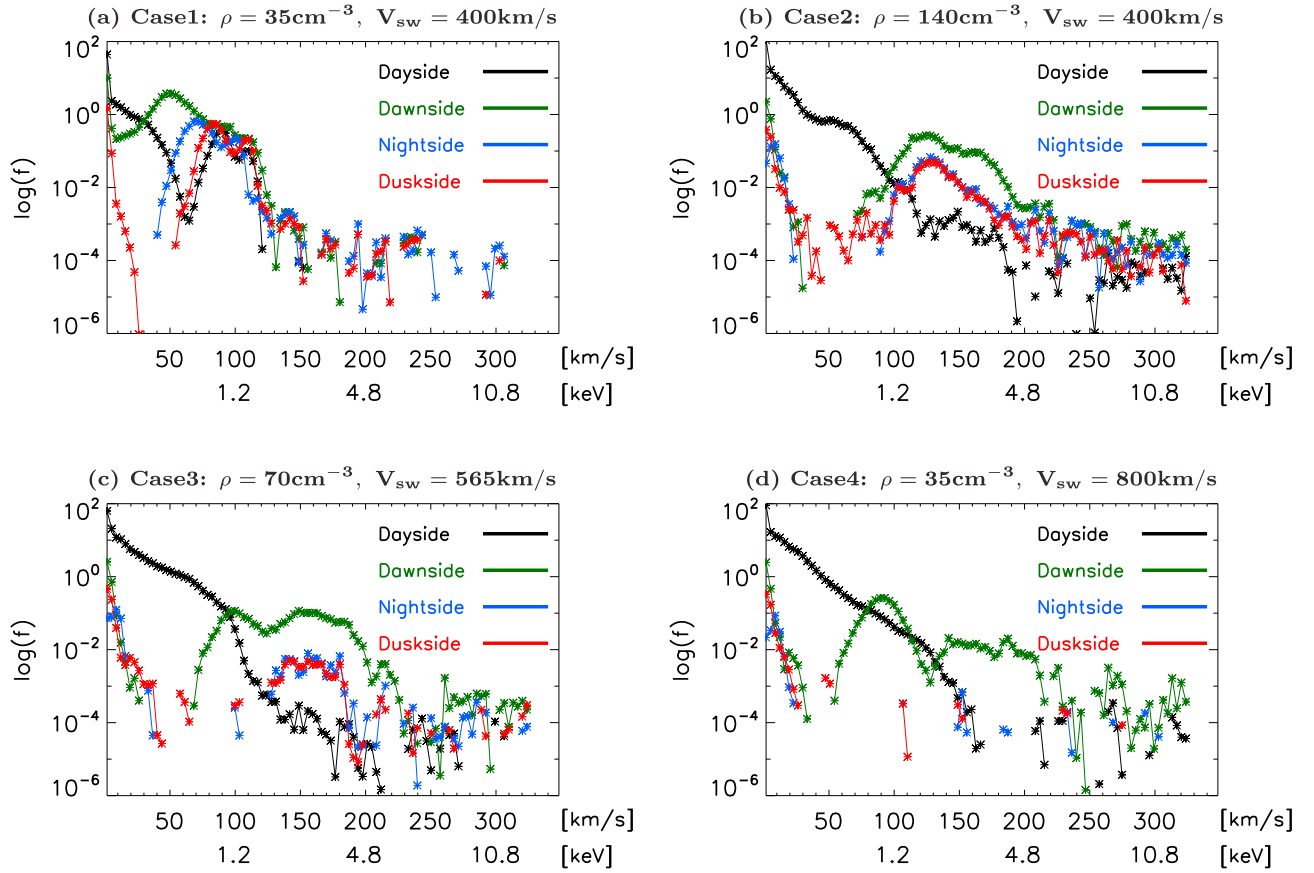
Figure 7. The results of statistical trajectory tracings of test sodium ions for Case 3. The format is the same as in Figure 5.

Pressure

(a)

(b)

Density

(c)

(d)

log(Pressure) [nPa]

log(Density) [cm⁻³]

Figure 8. The results of statistical trajectory tracings of test sodium ions for Case 4. The format is the same as in Figure 5.

Energy Distribution

Figure 9. Energy distributions sampled at $r = 1.0–1.3R_M$ around the planet. Each frame shows the distribution at MLT = 12 (black), 6 (green), 0 (blue), and 18 (red). (a) Case 1; (b) Case 2; (c) Case 3; and (d) Case 4.

(a) Case1: $\rho = 35\mathrm{cm}^{-3}$, $\mathrm{V_{sw}} = 400\mathrm{km/s}$
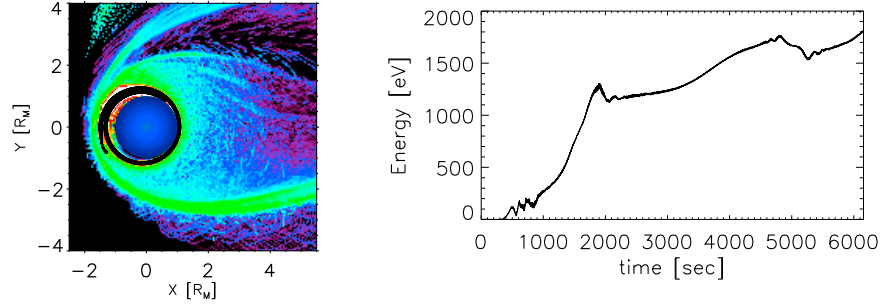
(b) Case2: $\rho = 140\mathrm{cm}^{-3}$, $\mathrm{V_{sw}} = 400\mathrm{km/s}$
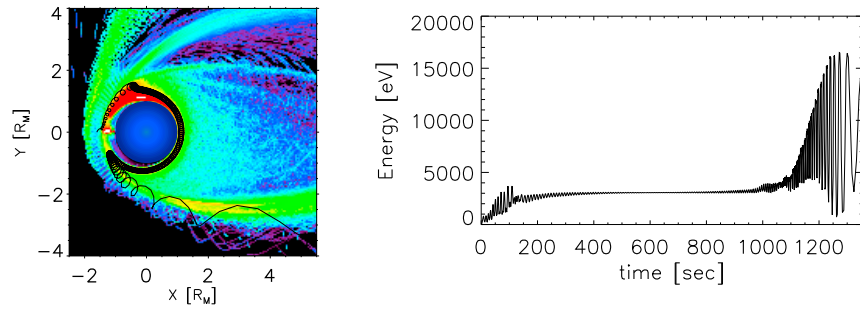
(c) Case3: $\rho = 70\mathrm{cm}^{-3}$, $\mathrm{V_{sw}} = 565\mathrm{km/s}$
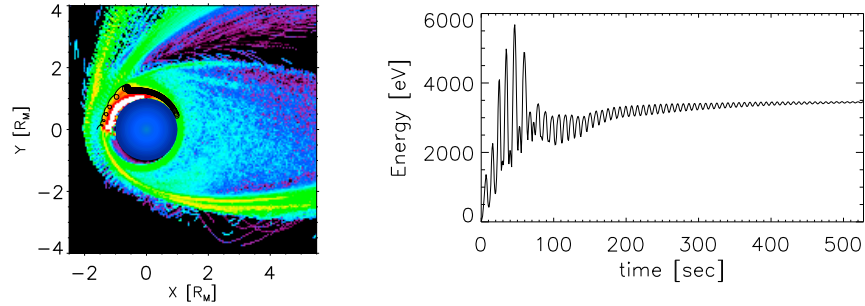
(d) Case4: $\rho = 35\mathrm{cm}^{-3}$, $\mathrm{V_{sw}} = 800\mathrm{km/s}$
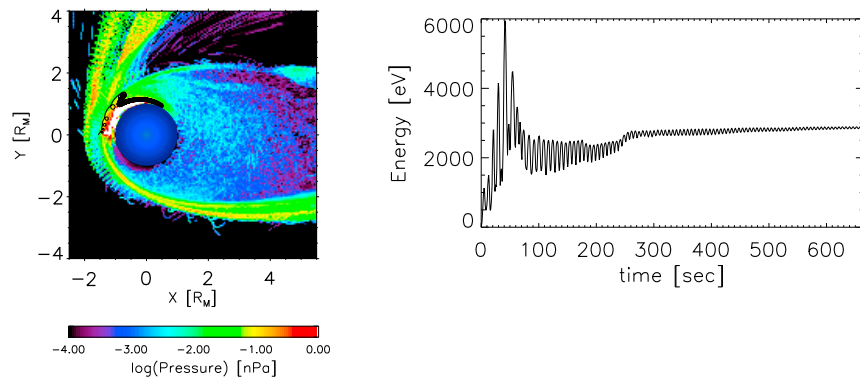
Figure 10. Examples of typical sodium ion trajectories in the equatorial plane (left) and time variation of its energy (right). (a) Case 1; (b) Case 2; (c) Case 3; and (d) Case 4.
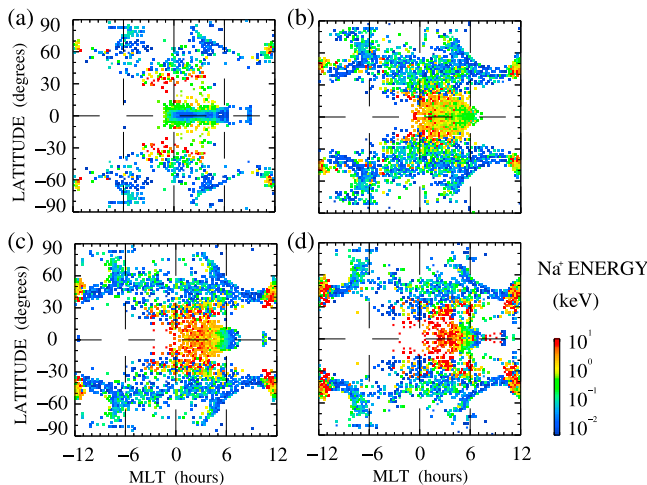
Figure 11. Profiles of precipitating sodium ions. The color code shows the energy of ions. The vertical axis is latitude and horizontal axis is MLT. (a) Case 1; (b) Case 2; (c) Case 3; and (d) Case 4.

[19] In Cases 2, 3, and 4 (Figures 10b, 10c, and 10d), particles are initially launched at $r = 1.6~R_M$, MLT = 12, LAT = 0, and E = 0 eV in the magnetosheath. The pickup ions in the sheath are accelerated up to a few keV in a few seconds. While drifting along the magnetopause, particles are meandering between the solar wind and the magnetosphere because of their large Larmor radius.

[20] Then the particles are transported into the magnetosphere by the magnetospheric convection. Once the particles get closer to the planet, they start to drift around the planet. These particles contribute to the formation of the high-pressure region. In Case 2, since the magnetopause is too close to the planet, high-energy particles cannot drift around the planet entirely, as in Case 1, and escape from the magnetosphere on the duskside. In Cases 3 and 4, the particles impact the planet while drifting in the nightside. Figure 11 shows the precipitation pattern of sodium ions onto the planet surface. Precipitation regions are formed by high-energy sodium ions in low-latitude region around 0 to 6 for MLT. Only a few ions precipitate before midnight because field lines of given magnetic field intensity are located at larger and larger distances from the planet, and so do magnetic drift paths. When the solar wind electric field becomes stronger, the precipitation region shifts to dawnside, which is consistent with the ion trajectories shown in Figure 10. The loss process is also consistent with the energy distributions in Figures 9b–9d, showing decreases of the high-energy populations from the dawnside to other local times along the drift paths.

4. Discussion

[21] The results of this statistical trajectory tracing for 4 different cases of solar wind conditions during northward IMF reveal the formation of a ring-shaped (or partial-ring shaped) high-pressure region around Mercury near the equator. Though the high-pressure region is formed in all cases and resembles that obtained in hybrid simulations [*Travnicek et al.*, 2007], the acceleration mechanisms are

different depending upon the solar wind dynamic pressure. The pattern presented in Figure 10 shows typical trajectories of particles contributing to this sodium ring. The acceleration process of the sodium ions is similar in Cases 2, 3, and 4 (that is, for high-pressure cases with various solar wind speed and density), but the shape of the sodium ring is different and is controlled by the entry points of the ions into the magnetosphere.

[22] These entry points are determined by two conditions. First, the magnetic gradient force at the magnetopause and magnetospheric convection must be balanced. The convection inside the magnetopause is 20–30 km/s at maximum, which is equivalent to the magnetic gradient drift of about 4 keV ion. Second, the Larmor radius of the ions should be larger than the width of the velocity shear layer, about 200–300 km, which is equivalent to the Larmor radius of about 1 keV ions at the magnetopause. Accordingly, the energy of particles that can enter the magnetosphere should be mostly within 1–4 keV, as reflected in the energy distribution (Figure 9).

[23] When the solar wind electric field becomes stronger, the ions in the magnetosheath are accelerated rapidly and reached 1 keV earlier. Accordingly, the entry point shifts to dayside, as shown in Figures 10b–10d. Once entering the magnetosphere, ∇B drift becomes dominant. Because the dayside magnetosphere is compressed and contour lines of magnetic field intensity are distorted, particles entering earlier on the dayside tend to impact the planet surface earlier while drifting toward nightside.

[24] To discuss the importance of exospheric ions on Mercury's magnetosphere, we have estimated their contribution to the pressure in the MHD simulation. Figure 12 shows the ratio of the sodium pressure to the MHD pressure in the equatorial plane. In the high-pressure region, the sodium ion pressure locally exceeds the MHD pressure (white color in Figure 12). The ratio of the sodium pressure to the MHD pressure at dawnside and nightside is summarized in Table 3. At dawnside, the sodium ion pressure is at least 10 percent in all cases and its contribution thus is not negligible. This suggests that the sodium current may effectively change the background MHD pressure. Similar to the ring current in the Earth's magnetosphere, it reduces the dipole field near the surface, and the ion motion may accordingly be altered. Still, the ratio of sodium ion pressure to magnetic pressure being less than 1, the essentially dipolar field lines should not be significantly modified. In other regions of the magnetosphere, the sodium ion contribution to the plasma pressure is less than 1 percent and is thus negligible.

[25] In this study, a steady solar wind condition with northward IMF is assumed. When the solar wind conditions change, Mercury's magnetosphere will respond within a few minutes [e.g., *Slavin and Holzer*, 1979] because of its small temporal and spatial scale. The lifetime of the ions constituting the sodium ring shown in this study ranges from several minutes to few hours. Therefore, the formation of the sodium ring described in this study should be valid only for steady solar wind conditions. Such extended periods of the solar wind with steady northward IMF are sometimes observed at Earth's orbit and are known to have specific effects on magnetospheric conditions, such as the formation of a cold dense plasma sheet [e.g., *Hasegawa et al.*, 2006,
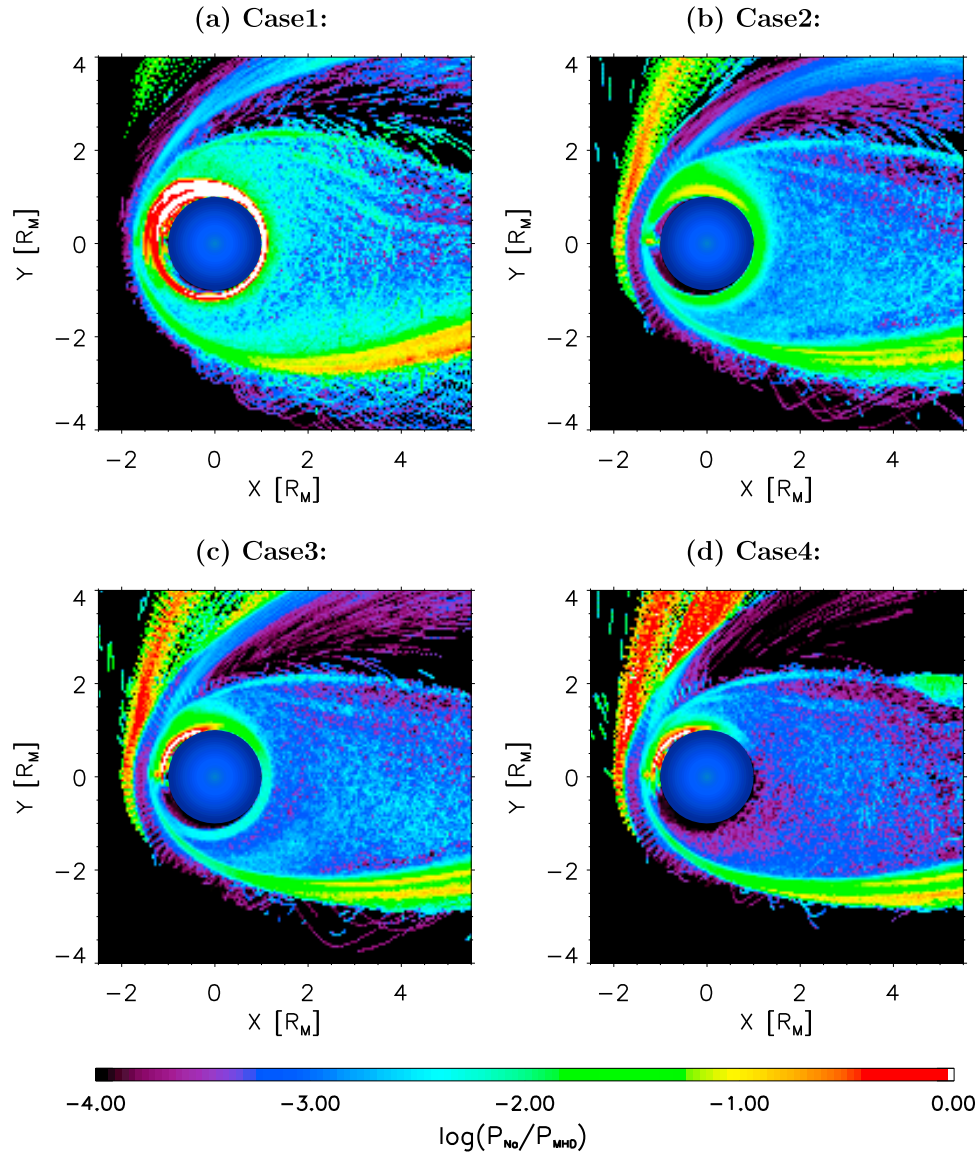
Figure 12. Ratio of the sodium ion pressure to the MHD pressure (P_{Na+}/P_{MHD}) in the equatorial plane. (a) Case 1; (b) Case 2; (c) Case 3; and (d) Case 4.

and references therein]. On the other hand, the important factor for the formation of a sodium ring is a steady return flow in the magnetosphere. Thus the sodium ring can also be formed under other steady conditions, such as Steady Magnetospheric Convection (SMC) occurring under southward IMF conditions [*O'Brien et al.*, 2002]. To discuss the possible effect of rapid changes of the magnetosphere, trajectory tracings using MHD field calculations with time variation will be needed.

5. Conclusion

[26] We performed statistical trajectory tracings of exospheric sodium ions in magnetic and electric field models obtained from global MHD simulations of Mercury's magnetosphere. While the results of the MHD simulation are in qualitative agreement with previous studies, a high-energy (up to 5 keV) sodium ring is formed around the planet near the equator, which was not formed in previous MHD simu-

lations. Two acceleration processes of the sodium ions are at the origin of this ring. One is acceleration picked up by the electric field of the magnetospheric convection, which is effective in the case of low dynamic pressure. The other is entry of the accelerated picked-up ions from the magnetosheath into the magnetosphere, which is effective in the case of high dynamic pressure. Subsequent magnetic drift of these accelerated ions in the vicinity of the planet leads to

Table 3. Maximum Ratio of the Sodium Pressure to MHD Proton Pressure Around the Planet at the Dawnside (MLT = 6)/Nightside (MLT = 0)

	V_{sw}		
ρ	400	565	800
35	2.4/1.7		0.097/0.0007
70		0.092/0.007	
140	0.12/0.03		

the formation of full or partial ring-shaped high-pressure regions around the planet. The contribution of the sodium ions to the total plasma pressure is not negligible in the vicinity of the planet, especially on the dawnside. On the other hand, their contribution is less than 1 percent of the total plasma pressure in other high-altitude regions, and the test particle scheme is valid in most parts of Mercury's magnetosphere. The acceleration mechanism in the magnetosheath can occur within a few minutes, while the acceleration by magnetospheric convection takes about half an hour. Since the typical drift period of these sodium ions is about a few to several tens of minutes, the appearance of the "sodium ring" highly depends on the steadiness of the solar wind. Observation of such a high-energy (~keV) sodium ions in the vicinity of the planet by the forthcoming MESSENGER and Bepi-Colombo missions may thus provide some clues on the coupling between Mercury's magnetosphere and the solar wind. More specific and realistic simulations that involve not only a steady state but also a time variation are needed in future works to investigate detailed magnetospheric responses.

References

Benna, M., et al. (2010), Modeling of the magnetosphere of Mercury at the time of the first MESSENGER flyby, *Icarus*, *209*, 3–10, doi:10.1016/j.icarus.2009.11.036.

Brackbill, J. U., and D. C. Barnes (1980), The effect of nonzero product of magnetic gradient and B on the numerical solution of the magnetohydrodynamic equations, *J. Comput. Phys.*, *35*, 426–430, doi:10.1016/0021-9991(80)90079-0.

Delcourt, D. C., S. Grimald, F. Leblanc, J. Berthelier, A. Millilo, A. Mura, S. Orsini, and T. E. Moore (2003), A quantitative model of the planetary Na+ contribution to Mercury's magnetosphere, *Ann. Geophys.*, *21*, 1723–1736.

Delcourt, D. C., K. Seki, N. Terada, and Y. Miyoshi (2005), Electron dynamics during substorm dipolarization in Mercury's magnetosphere, *Ann. Geophys.*, *23*, 3389–3398.

Delcourt, D. C., F. Leblanc, K. Seki, N. Terada, T. E. Moore, and M. Fok (2007), Ion energization during substorms at Mercury, *Planet. Space Sci.*, *55*, 1502–1508, doi:10.1016/j.pss.2006.11.026.

Eraker, J. H., and J. A. Simpson (1986), Acceleration of charged particles in Mercury's magnetosphere, *J. Geophys. Res.*, *91*, 9973–9993, doi:10.1029/JA091iA09p09973.

Hasegawa, H., M. Fujimoto, K. Takagi, Y. Saito, T. Mukai, and H. Rème (2006), Single-spacecraft detection of rolled-up Kelvin-Helmholtz vortices at the flank magnetopause, *J. Geophys. Res.*, *111*, A09203, doi:10.1029/2006JA011728.

Ip, W. (1987), Dynamics of electrons and heavy ions in Mercury's magnetosphere, *Icarus*, *71*, 441–447, doi:10.1016/0019-1035(87)90039-X.

Ip, W., and A. Kopp (2002), MHD simulations of the solar wind interaction with Mercury, *J. Geophys. Res.*, *107*(A11), 1348, doi:10.1029/2001JA009171.

Kabin, K., T. I. Gombosi, D. L. DeZeeuw, and K. G. Powell (2000), Interaction of Mercury with the solar wind, *Icarus*, *143*, 397–406, doi:10.1006/icar.1999.6252.

Kabin, K., M. H. Heimpel, R. Rankin, J. M. Aurnou, N. Gómez-Pérez, J. Paral, T. I. Gombosi, T. H. Zurbuchen, P. L. Koehn, and D. L. Dezeeuw (2008), Global MHD modeling of Mercury's magnetosphere with applications to the MESSENGER mission and dynamo theory, *Icarus*, *195*, 1–15, doi:10.1016/j.icarus.2007.11.028.

Kallio, E., and P. Janhunen (2003), Modelling the solar wind interaction with Mercury by a quasi-neutral hybrid model, *Ann. Geophys.*, *21*, 2133–2145.

Kameda, S., I. Yoshikawa, M. Kagitani, and S. Okano (2009), Interplanetary dust distribution and temporal variability of Mercury's atmospheric Na, *Geophys. Res. Lett.*, *36*, L15201, doi:10.1029/2009GL039036.

Kidder, A., R. M. Winglee, and E. M. Harnett (2008), Erosion of the dayside magnetosphere at Mercury in association with ion outflows and flux rope generation, *J. Geophys. Res.*, *113*, A09223, doi:10.1029/2008JA013038.

Killen, R. M., and W. Ip (1999), The surface-bounded atmospheres of Mercury and the Moon, *Rev. Geophys.*, *37*, 361–406, doi:10.1029/1999RG900001.

Leblanc, F., and R. Johnson (2010), Mercury exosphere: I. Global circulation model of its sodium component, *Icarus*, *209*, 280–300, doi:10.1016/j.icarus.2010.04.020.

Leblanc, F., and R. E. Johnson (2003), Mercury's sodium exosphere, *Icarus*, *164*, 261–281, doi:10.1016/S0019-1035(03)00147-7.

Leblanc, F., D. Delcourt, and R. E. Johnson (2003), Mercury's sodium exosphere: Magnetospheric ion recycling, *J. Geophys. Res.*, *108*(E12), 5136, doi:10.1029/2003JE002151.

Lundin, R., S. Barabash, P. Brandt, L. Eliasson, C. M. C. Nairn, O. Norberg, and I. Sandahl (1997), Ion acceleration processes in the Hermean and terrestrial magnetospheres, *Adv. Space Res.*, *19*, 1593, doi:10.1016/S0273-1177(97)00373-6.

McClintock, W. E., E. T. Bradley, R. J. Vervack, R. M. Killen, A. L. Sprague, N. R. Izenberg, and S. C. Solomon (2008), Mercury's exosphere: Observations during MESSENGER's first Mercury flyby, *Science*, *321*, 92, doi:10.1126/science.1159467.

Mura, A., A. Milillo, S. Orsini, and S. Massetti (2007), Numerical and analytical model of Mercury's exosphere: Dependence on surface and external conditions, *Planet. Space Sci.*, *55*, 1569–1583, doi:10.1016/j.pss.2006.11.028,.

Ness, N. F., K. W. Behannon, R. P. Lepping, and Y. C. Whang (1975), The magnetic field of Mercury: I, *J. Geophys. Res.*, *80*, 2708–2716, doi:10.1029/JA080i019p02708.

O'Brien, T. P., S. M. Thompson, and R. L. McPherron (2002), Steady magnetospheric convection: Statistical signatures in the solar wind and AE, *Geophys. Res. Lett.*, *29*(7), 1130, doi:10.1029/2001GL014641.

Ogilvie, K. W., J. D. Scudder, V. M. Vasyliunas, R. E. Hartle, and G. L. Siscoe (1977), Observations at the planet Mercury by the plasma electron experiment: Mariner 10, *J. Geophys. Res.*, *82*, 1807–1824, doi:10.1029/JA082i013p01807.

Potter, A., and T. Morgan (1985), Discovery of sodium in the atmosphere of Mercury, *Science*, *229*, 651–653, doi:10.1126/science.229.4714.651.

Potter, A. E., and T. H. Morgan (1997), Evidence for suprathermal sodium on Mercury, *Adv. Space Res.*, *19*, 1571, doi:10.1016/S0273-1177(97)00370-0.

Potter, A. E., R. M. Killen, and T. H. Morgan (2002), The sodium tail of Mercury, *Meteor. Planet. Sci.*, *37*, 1165–1172.

Sarantos, M., J. A. Slavin, M. Benna, S. A. Boardsen, R. M. Killen, D. Schriver, and P. Trávníček (2009), Sodium-ion pickup observed above the magnetopause during MESSENGER's first Mercury flyby: Constraints on neutral exospheric models, *Geophys. Res. Lett.*, *36*, L04106, doi:10.1029/2008GL036207.

Siscoe, G. L., N. F. Ness, and C. M. Yeates (1975), Substorms on Mercury, *J. Geophys. Res.*, *80*, 4359–4363, doi:10.1029/JA080i031p04359.

Slavin, J. A. (2009), MESSENGER Observations of magnetic reconnection in Mercury's magnetosphere, *Science*, *324*, 606, doi:10.1126/science.1172011.

Slavin, J. A. (2004), Mercury's magnetosphere, *Adv. Space Res.*, *33*, 1859–1874, doi:10.1016/S0273-1177(04)00009-2.

Slavin, J. A., and R. E. Holzer (1979), The effect of erosion on the solar wind standoff distance at Mercury, *J. Geophys. Res.*, *84*, 2076–2082, doi:10.1029/JA084iA05p02076.

Slavin, J. A., et al. (2008), Mercury's magnetosphere after MESSENGER's first flyby, *Science*, *321*, 85–89, doi:10.1126/science.1159040.

Travnicek, P., P. Hellinger, and D. Schriver (2007), Structure of Mercury's magnetosphere for different pressure of the solar wind: Three-dimensional hybrid simulations, *Geophys. Res. Lett.*, *34*, L05104, doi:10.1029/2006GL028518.

Whang, Y. C. (1977), Magnetospheric magnetic field of Mercury, *J. Geophys. Res.*, *82*, 1024–1030, doi:10.1029/JA082i007p01024.

Xiao, F., T. Yabe, G. Nizam, and T. Ito (1996), Constructing a multidimensional oscillation preventing scheme for the advection equation by a rational function, *Comput. Phys. Commun.*, *94*, 103–118, doi:10.1016/0010-4655(96)00008-2.

Yabe, T., and T. Aoki (1991), A universal solver for hyperbolic equations by cubic-polynomial interpolation I. One-dimensional solver, *Comput. Phys. Commun.*, *66*, 219–232, doi:10.1016/0010-4655(91)90071-R.

Yabe, T., F. Xiao, and T. Utsumi (2001), The constrained interpolation profile method for multiphase analysis, *J. Comput. Phys.*, *169*, 556–593, doi:10.1006/jcph.2000.6625.

Yagi, M., K. Seki, and Y. Matsumoto (2009), Development of a magneto-hydrodynamic simulation code satisfying the solenoidal magnetic field condition, *Comput. Phys. Commun.*, *180*, 1550–1557, doi:10.1016/j.cpc.2009.04.010.

D. C. Delcourt, Laboratoire de Physique des Plasmas, Ecole Polytechnique-CNRS, Observatoire de Saint-Maur, 4 Avenue de Neptune, F-94107 Saint Maur des Fosses, France.

F. Leblanc, LATMOS/IPSL, Universitè Versailles Saint Quentin, CNRS, F-91371 Verrières-le-Buisson, France.

Y. Matsumoto, K. Seki, and M. Yagi, Solar-Terrestrial Environment Laboratory, Nagoya University, Furocho, Chikusa-ku, Nagoya, Aichi 464-8601, Japan. (yagi@stelab.nagoya-u.ac.jp)